Confinement Effects on a Supersonic Hydrogen Jet Flame in a Duct

Lukas Gaipl, Thierry Poinsot

Confinement Effects on a Supersonic Hydrogen Jet Flame in a Duct

Lukas Gaipl[a,*] and Thierry Poinsot[b]

[a] *CERFACS, 42 Avenue Gaspard Coriolis, 31057 Toulouse, France*
[b] *IMFT, Université de Toulouse, CNRS, 31400 Toulouse, France*

24 January 2025

Abstract

This study investigates high-speed, confined hydrogen-air jet flames, representative of leak scenarios from a high pressure hydrogen tank in practical applications. Using high-fidelity Large Eddy Simulation (LES) with detailed combustion chemistry and heat transfer modeling, the research examines a round supersonic jet flame confined within a duct, subjected to an air crossflow and impinging on the duct walls. The confined hydrogen jet flame interacts strongly with its surroundings [1], leading to significant thermal stresses and accelerated wall degradation. Two configurations are compared: Case W, where the flame has sufficient space to ignite and develop before interacting with the opposite wall [2], and Case N, where the nozzle-to-plate spacing is smaller than the flame lift-off height, resulting in partial flame quenching due to confinement. Substantial differences are observed between cases W and N. For Case W, the flame is attached to the jet, exhibits a central premixed core followed by a stabilized diffusion zone like in free jet flames. For Case N, this jet region is quenched. However, the overall flame does not extinguish and combustion proceeds in a large diffusion flame, stabilized away from the jet. Case N also exhibits increased heat loads on the walls and higher quantities of unburnt hydrogen exiting the duct compared to Case W.

Keywords: Conjugate Heat Transfer; Safety; Flame/Wall Interaction, LES, Jet Flame in Crossflow

1) Novelty and Significance Statement

Supersonic hydrogen jet flames (issuing from a high-pressure tank through a nozzle) are usually studied in free space. Recent safety concerns for hydrogen leaks require to study how hydrogen jets will behave in very confined setups, where the nozzle exit to plate spacing is smaller than the nominal lift-off height of the jet flame. The investigation of these hydrogen jets into small ducts is crucial for safety in future hydrogen applications. This work presents the first detailed simulation of cases where the supersonic hydrogen jet is strongly confined in a duct. It shows that, for very small nozzle to plate spacings, hydrogen does not burn in the shear layer of the jet but diffuses and burns far away from the jet core, creating a new flame topology and different wall heat loads compared to standard free flames and classical impinging jets.

2) Author Contributions

- L. G.: Writing - original draft, designed research, performed research, analyzed data
- T. P.: Writing - review & editing, designed research, supervision

1. Introduction

The increasing use of hydrogen in combustion applications raises safety concerns caused by short ignition times, wide flammability limits and low minimum ignition energy [1–3]. Two key safety scenarios can be distinguished by their ignition timing when gas leaks from a hole of diameter D: (1) delayed ignition, where the accumulation of flammable hydrogen air mixtures results in deflagrations or explosions [4–7], and (2) immediate ignition, leading to a jet flame, stabilized on the supersonic hydrogen jet, with significant heat transfer to its surroundings [8]. The present numerical work focuses on the second type of event where it is assumed that ignition will take place immediately and a hydrogen jet flame will start burning.

Most hydrogen leaks will issue from high-pressure tanks (P_i = 1 to 900 bars) for which three jet states can occur: (a) subsonic [9, 10], (b) critical [11, 12], and (c) supersonic jets [13, 14]. If the tank pressure P_i is above the critical pressure (approximately 1.9 bar for hydrogen) and the leak flows into an atmospheric domain, the exit flow chokes and an underexpanded jet forms. It is characterized by a complex shock structure and a non-uniform velocity distribution [15]. The jet core is dominated by large, regular vortices induced by turbulence, that mix jet and ambient fluid [16]. If these jets are confined, heat transfer must be studied to evaluate, whether walls can withstand the flame heat loads and if so, for how long.

Reactive impinging jets have been documented for years [17–19] and are found in an expanding range of industrial heating processes and safety scenarios. While classical industrial furnaces transfer heat to the stock mainly by radiation, direct flame impingement has become more popular due to the possibility of saving energy and improving the quality of the hot product [20]. Impinging jets are subdivided into three regions [21] (Fig. 1):

- 1) free jet region, where ambient air is entrained to the jet plume driven by shear,
- 2) stagnation region, where the jet turns into radial direction leading to a thin thermal boundary layer,
- 3) wall jet region, where the jet moves laterally parallel to the wall.

The reaction zone is usually located in the free jet region and is lifted by a distance L. When the burnt gases reach the opposite wall, they generate very high heat fluxes, of the order of MW/m^2 which can destroy the wall rapidly. Chemical species created in the jet flame, diffuse and recombine near the wall, leading to elevated heat fluxes [22]. For sufficiently small nozzle to plate spacing L_z, the central jet core remains colder than the maximum temperature observed radially outside [23]. The dominant mode of heat transfer to the walls is forced convection and radiation is usually found to account for 2 % of total heat transfer [24]. Recombination of radicals in the boundary layer of the cooled impingement surface can account for up to 20 % of the total heat release [23, 25]. Heat fluxes are maximum when the nozzle-to-wall distance L_z coincides with the length of the potential jet core L_{sc} [26, 27]. It additionally depends on the jet Reynolds number and equivalence ratio [28].

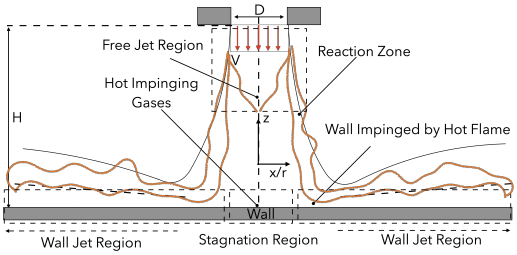

Fig. 1: Schematic structure of an impinging jet flame.

Most studies were performed by employing a jet of combustible CH_4-air or CH_4-oxygen mixtures [1] and average heat transfer coefficients were found to increase by a factor of three for direct impinging flames when compared to non-reactive impinging gas jets [29, 30]. Data for supersonic impinging hydrogen jet flames is sparse and most previous research was conducted for open configurations [31]. Higher wall fluxes are expected as for hydrocarbon flames and the effect of the intrinsic properties of hydrogen are not well understood.

This paper aims to simulate the flame structure, stabilisation and heat transfer characteristics of a supersonic hydrogen jet flame in very confined setups as found in multiple safety scenarios. It is structured as follows: the geometry and boundary conditions are described in Section 2 while the numerical setup is presented in Section 3. The flames structure and the distribution of wall heat fluxes are investigated in Section 4 for two extreme cases: a 'wide' case called W where the nozzle-to-wall distance L_z is large compared to the lift-off height L of the free flame and a 'narrow' case called N where L_z is smaller than L. Results are summarized in Section 5. For these flames, which combine shocks and small reaction zones, resolution is an issue and grid independence is discussed in Annex 1.

2. Configuration

The geometry (Fig. 2) is a generic rectangular wind tunnel of $L_x = 612$ mm length and $L_y = 120$ mm width. L_z is either 90mm for Case W or 20 mm for Case N. Air at standard conditions ($p = 1.01325$ Pa, $T = 300$ K) is injected at the tunnel inlet with a velocity of $u = 2$ m/s. A convergent circular nozzle with a $D = 1.5$ mm diameter is installed on the bottom wall, 253 mm downstream of the tunnel entrance, to inject pure hydrogen from a tank at a constant pressure $P_i = 5$ bar and a temperature of $T = 300$ K.

The two cases W and N were chosen in the following way: for Case W, the tunnel height L_z should be

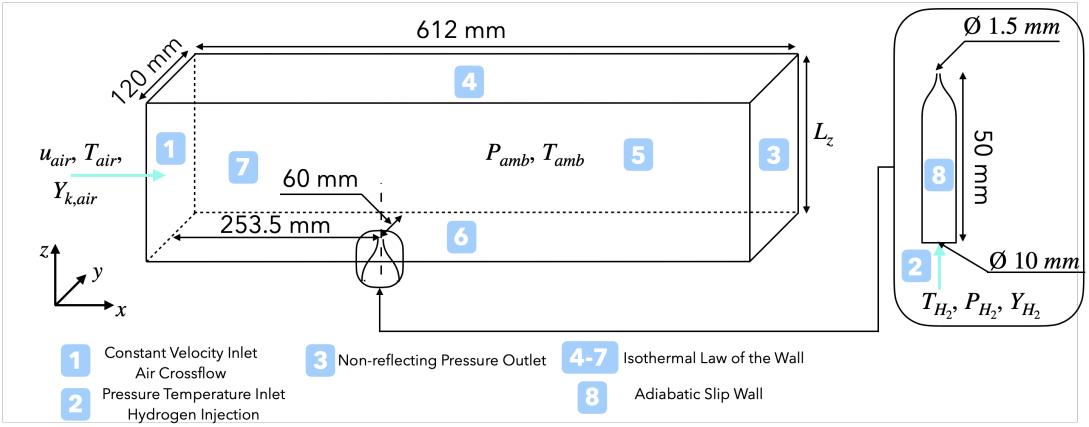

Fig. 2: Setup and boundary conditions. The tunnel height is $L_z = 20$ mm for Case N and $L_z = 90$ mm for Case W.

larger than the reference lift-off height of the free jet flame L; for Case N, L_z would be less than L so that the upper wall will modify the jet region. The flame lift-off height L was estimated from empirical correlations [2, 32]:

$$L/D = -0.0002U^* + 0.19U^* - 3.3/f, \quad (1)$$

where D is the jet exit diameter, $P_i = 5 \cdot 10^5$ Pa and $P_a = 1.013 \cdot 10^5$ Pa are the tank and the ambient pressure respectively. $f = (X_{fuel}/X_{air})|_{s_{L,max}} = 0.756$ is the ratio of fuel to air moles in the fuel air mixture for maximum $s_L = 3.07$ m/s for H_2/air mixtures at ambient conditions ($\phi = 1.8$). U^* is the jet flow parameter defined as:

$$U^* = \left(\frac{u}{s_L}\right)\left(\frac{\delta}{D}\right)^{0.4}\left(\frac{P_i}{P_a}\right). \quad (2)$$

Eq. 1 leads to a nominal lift-off height $L = 48$ mm for a free flame, so that L_z was set to 90 mm for Case W and 20 mm for Case N.

A second reference length for the underexpanded hydrogen jet is the length of the jet potential core L_{sc}, i.e. the length of the nozzle exit to the point where the mixing layer merges on the central axis of the jet [26, 27]. For hydrogen, the only available quantitative results deal with the supersonic core length L_{sc} [33], defined as the distance from the nozzle exit to the axial location along the centerline, where the local flow Mach number drops below $M = 1.0$. An evaluation of L_{sc} [33] gives:

$$L_{sc}/D = 1.8P_i/P_a + 2.9, \quad (3)$$

For our configurations, $L_{sc} = 18$ mm so that Case N will correspond to a case where the tunnel height is less than the lift-off height L but also close to the size L_{sc} of the shock system created at the nozzle outlet, leading to strong confinement effects.

Simulation parameters for cases W and N are summarized in Table 1, where the tunnel's Reynolds number is defined as $Re_{tu} = (u_{air}H_{tu}\rho)/\eta_{air}$.

Table 1: Case Overview

Description (units)	Case N	Case W
Tunnel height L_z (mm)	20	90
Tunnel width L_y (mm)	120	
Hydrogen flow rate (g/s)	0.54	
Power (kW)	65.3	
Air flow rate (g/s)	5.64	25.4
Reynolds of air flow Re_{tu} (-)	1400	6600
Global equivalence ratio (-)	0.77	0.17

3. Numerical Setup

Large eddy simulations are performed with the fully compressible solver AVBP [34] running on GPUs. The Navier-Stokes equations are solved explicitly in time. To discretize the convective terms on a finite volume basis, a third-order Taylor-Galerkin scheme is applied, while a second-order Galerkin scheme for finite elements is used for diffusion terms [35]. Velocity sub-grid stress terms are calculated with the WALE model [36] while gradients in insufficiently resolved mesh regions are treated via an artificial viscosity sensor for reacting flows [37]. A local artificial diffusion approach with a sensor based on pressure discontinuities [38] is employed to smear large gradients induced by shock waves. Chemical source terms are computed with the San Diego scheme (9 species, 21 reactions) [39]. To resolve turbulence chemistry interactions, flames are dynamically thickened using a sensor tracking the local reaction rate [40]. Subgrid scale (SGS) turbulent flame wrinkling is accounted for by Charlette's efficiency function [41] and SGS thermodiffusive instabilities are modeled via a SGS model proposed by Aniello et al. [42]. Model parametrisation errors due to differential diffusion effects across the flame front are accounted for by the multi-fuel TFLES extension [43]. Flame thickening is only applied to premixed flame branches using Takeno conditioning [44] as done successfully in other studies [45–47].

Boundary conditions use the NSCBC formalism [49]. A coupled wall law is used on the walls of

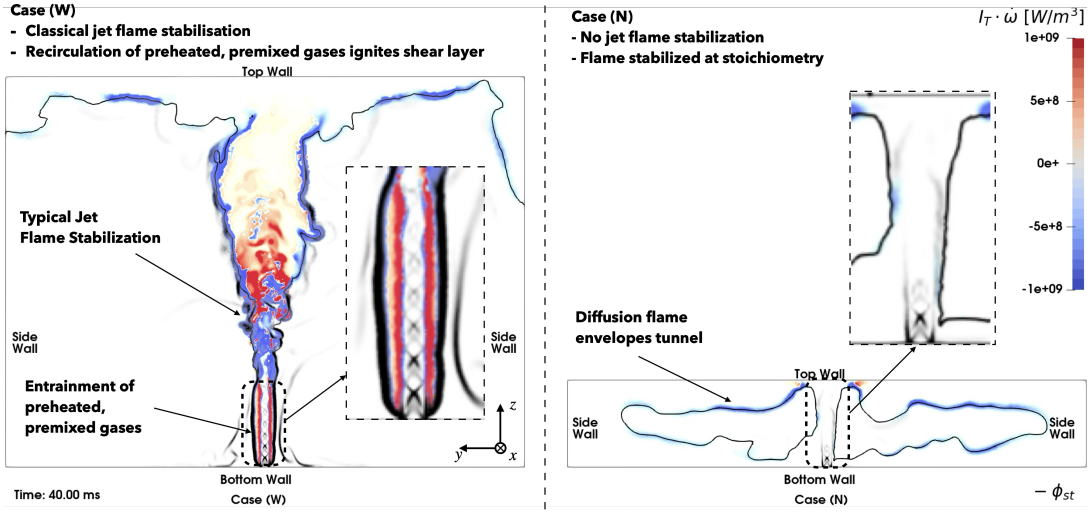

Fig. 3: Flame stabilization in the transverse yz-plane (see Fig. 2) for stabilized conditions indicated by the Takeno index [48] multiplied with the heat release rate. Left: Case W, right: Case N. Blue structures refer to diffusion flames and red ones to premixed ones. Zooms on the nearfield zone of the jets are provided.

the duct to account for density and temperature variations as well as for molecular Prandtl number effects. The velocity profile is based on the Van Driest transformation [50]:

$$u^+_{VD} = \frac{1}{k} \ln y^+ + 5.5, \tag{4}$$

where $k = 0.41$. The expression for the temperature profile reads:

$$T^+ = (Pry^+)e^{\Gamma} + (Pr_t u^+ + \beta(\mathrm{Pr}))e^{1/\Gamma}, \tag{5}$$

where the constant:

$$\beta(\mathrm{Pr}) = (3.85\,\mathrm{Pr}^{1/3} - 1.2)^2 + 2.12 \ln \mathrm{Pr} \tag{6}$$

accounts for changes in the molecular Prandtl number. Γ is a function that smoothes the T^+ profile between laminar and turbulent parts:

$$\Gamma = -0.01 \frac{(Pry^+)^4}{1 + 5Pr^3 y^+} \tag{7}$$

This law-of-the-wall is built so that results agree with the Kader law [51] for negligible temperature and density variations [52]. It was developed for a turbulent Prandtl number $\mathrm{Pr}_t = 0.85$. Thermodynamic properties are computed for wall conditions that are controlled by the imposed wall temperature.

4. Results

This section describes the LES results for cases W and N and focuses on the differences in flame structure and heat transfer dynamics between the two setups. Flame stabilization and mixing are analyzed in Section 4.1 using instantaneous solutions to examine key features such as flame anchoring, shape, and the interaction of the flame with the surrounding flow field. Heat transfer to all tunnel walls is explored in Section 4.2 to understand the impact of confinement on the thermal loads of the duct.

4.1. Flame Stabilization and Mixing

Both Cases N and W reach a quasi steady state after 40 ms. To understand the stabilization modes of these flames, various diagnostics are needed. First, the heat release rate $\dot{\omega}$ conditioned by the Takeno index I_T [48] is used:

$$I_T = \frac{\nabla Y_O \cdot \nabla Y_F}{|\nabla Y_O \cdot \nabla Y_F|}, \tag{8}$$

where Y_F and Y_O are fuel and oxidizer mass fractions, respectively. Negative values (blue) thus indicate a diffusion flame, while positive values (red) highlight premixed flames. Instantaneous solutions of Takeno-conditioned heat release and of Schlieren images in a front view (yz-plane cut) are shown in Figure 3 for both cases at $t = 40$ ms, where both flames are stabilized and do not move any more. Numerical Schlieren visualize the shock structure in the near field of the supersonic H_2 jet, indicating a diamond shock structure as expected for a moderately underexpanded jet. The shock structures are more pronounced for Case W than for Case N.

In Case W, the flame exhibits stabilization characteristics similar to a classical underexpanded jet flame: the flame is lifted and premixing of hydrogen and air takes place at the jet outlet. These premixed gases burn in a Bunsen type V flame along the central axis, while diffusion flame branches form at the stoichiometric interface between fuel and air. This rather usual flame structure then meets the upper duct wall and the hot gases impinge the top wall of the tunnel,

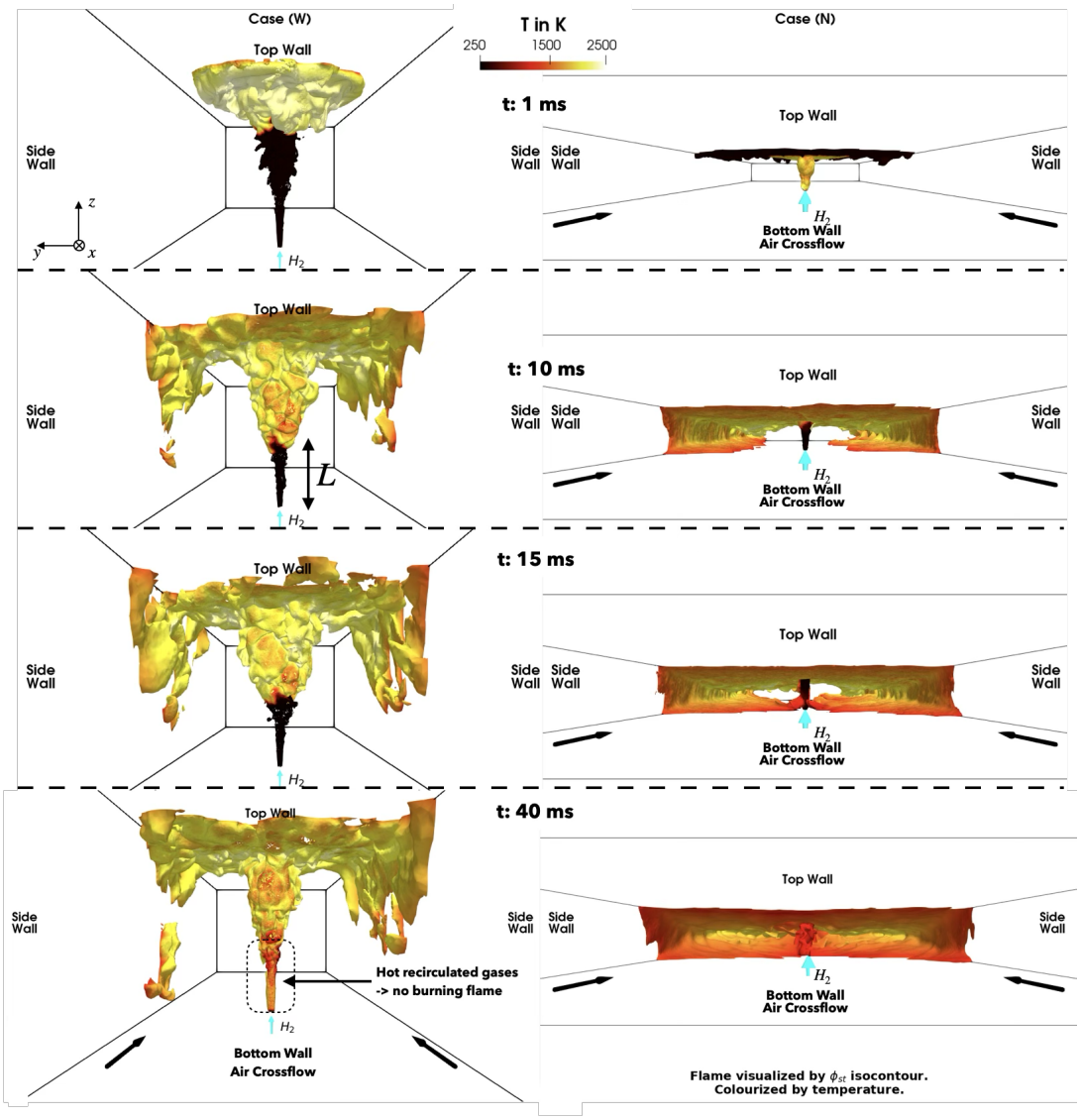

Fig. 4: Three dimensional visualization of the flame front for Case W and Case N from a front view (yz-Plane) perspective. The $z = z_{st}$ isosurface is colored by temperature: black zones correspond to a non-burning state (for example the lift-off region). A video is available in the supplementary materials.

turn at 90 degrees parallel to the tunnel ceiling like in a stagnation point flow. They fill up the cross section of the duct and are transported downstream by the air cross flow. Combustion predominantly occurs within the rich premixed core of the jet, far from the top wall. A video visualizing this behaviour is added to the supplementary materials of this paper.

For Case N, a different flame structure is observed: the top wall is so close to the jet exit that the flame has not enough space to ignite and stabilize: the reaction zone expected on the shear layer between air and hydrogen, seen for Case W, is quenched. The overall flame, however, does not extinguish and combustion takes place further away from the jet exit, somewhere else in the channel: diffusion flames burn all around the tunnel walls, including near the bottom wall. The channel fills with burnt gases and the heat release is distributed evenly around the stoichiometric isocontour.

Figure 3 illustrates the steady-state configuration reached by the two flames. However, it is also interesting to examine the transient evolution of the flames, from the moment of ignition to the establishment of the steady state. This is done in Figure 4 where the temporal development of the flame front of cases W and N is depicted in 3D by the $z = z_{st}$-

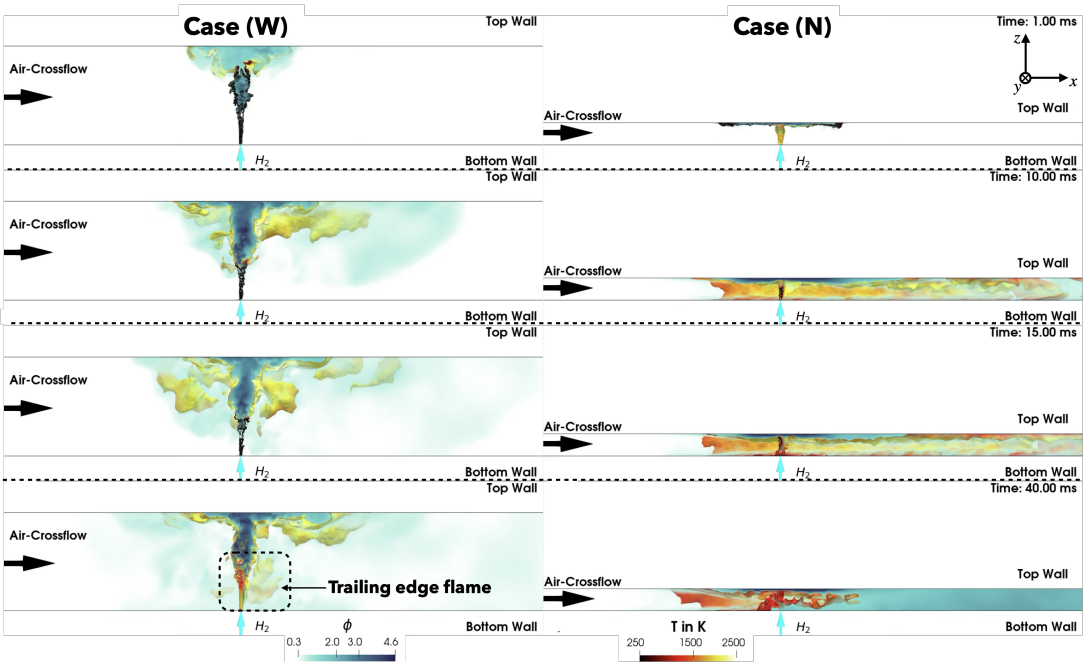

Fig. 5: Three-dimensional visualization of flame front and flammable mixture for Case W and Case N from a side view (xz-plane). The flame front is visualized by the $z = z_{st}$ isocontour coloured by temperature and H_2 is conditioned to flammable mixtures ($0.3 < \phi < 4.6$). A video is available in the supplementary materials.

isocontour coloured by temperature, also in a front view perspective (yz-plane). Case W is ignited at the ceiling and exhibits features of a classical impinging jet flame (Fig. 1). After $t = 10$ ms, the flame is stabilized at a lift-off height L above the nozzle exit. It impinges the top wall, where it turns parallel to the wall. The jet core then pushes the rich mixture around the tunnel walls until the side walls of the duct are reached and the flame turns downwards ($t = 15$ ms). The flame then stabilizes, burning at the top and side walls of the duct. In the steady state, the jet flame is still stabilized at a lift-off height L, however hot gases recirculate from the side walls and heat the shear layer of the jet core, leading to increased temperatures and initial reactions in the near field of the jet. However, the main flame stays stabilized at its lift-off height L.

The time evolution of Case N is different: after ignition near the duct centre, the flame quenches rapidly in the jet shear layers and moves from the nozzle exit towards the tunnel ceiling. After $t = 10$ ms the flame approaches the bottom wall and burns in a circular manner, enveloping all tunnel walls. At $t = 15$ ms, the flame touches the jet core of pure hydrogen, so that the shear layer of the jet itself is heated. In the final state ($t = 40$ ms, bottom images in Fig. 4), the flame shows a closed conical structure at the interface of rich mixture at the duct walls and air in the duct centre provided by the air cross flow.

Figure 5 presents a 3D visualization of the mixing behaviour for both cases, illustrating the distribution of hydrogen-air mixtures within the flammability range at ambient conditions ($\phi_{LFL} = 0.3 < \phi < \phi_{UFL} = 4.6$) in a side view (xz-plane clip). In both scenarios, a jet of rich gases impacts the tunnel ceiling, resulting in radial outward spreading and parallel flow along the tunnel walls. Upon reaching the side walls (y-direction), the flow redirects toward the tunnel floor, as depicted in Figure 4.

For Case W, flammable mixtures envelop the ceiling and sidewalls after $t = 10$ ms. Subsequently, preheated flammable gases descend to the tunnel floor, where they recirculate, heat the jet core, and are carried downstream ($t = 15$ ms). A flame stabilizes in the wake of the jet's nearfield due to the presence of preheated flammable mixtures, enabling sustained combustion ($t = 40$ ms).

In contrast, for Case N, the flammable mixture rapidly spreads along the four tunnel walls. In the axial direction, the flame front propagates toward the tunnel outlet, with a faster progression observed than for Case W. By $t = 10$ ms, the flame has fully enveloped the tunnel walls. The flammable hydrogen-air mixture is distributed throughout the tunnel and continues to convect downstream toward the outlet. At $t = 40$ ms, Case N displays a conical flame burning at stoichiometric conditions due to rich hydrogen air mixture that is observed all around the tunnel walls downstream the jet. A video is available in the supplementary materials of this work.

Overall, the air cross flow has a minor influence in the near-field of the jet for both cases as expected

based on the jet-to-crossflow momentum ratio:

$$R = \frac{\rho_F \cdot u_F^2}{\rho_{CF} \cdot u_{CF}^2} = 1.7 \cdot 10^5, \tag{9}$$

that indicates a jet-dominated regime [53] and explains why the hydrogen jet almost does not bend before hitting the opposite wall for Cases W and N. Away from the jet, the air cross flow pushes all gases downstream towards the outlet.

Clearly, combustion is less efficient for Case N because the duct is filled with burnt gases and the main combustion mode is diffusion. This can be quantified by measuring the combustion inefficiency η of the two flames, defined by the unburnt hydrogen flow rate leaving the duct, divided by the injected hydrogen flow rate $\eta = \dot{m}_{H_2,out}/\dot{m}_{H_2,in}$. After stabilization, this inefficiency is 1 percent for Case W but reaches 28 percent for Case N: the narrow duct of Case N is not able to burn all the injected hydrogen and a significant part of it is ejected at the duct outlet, constituting another safety hazard, because the exhaust gases leaving the duct will be hot and still contain hydrogen.

4.2. Heat Transfer Analysis and Wall Heat Loads

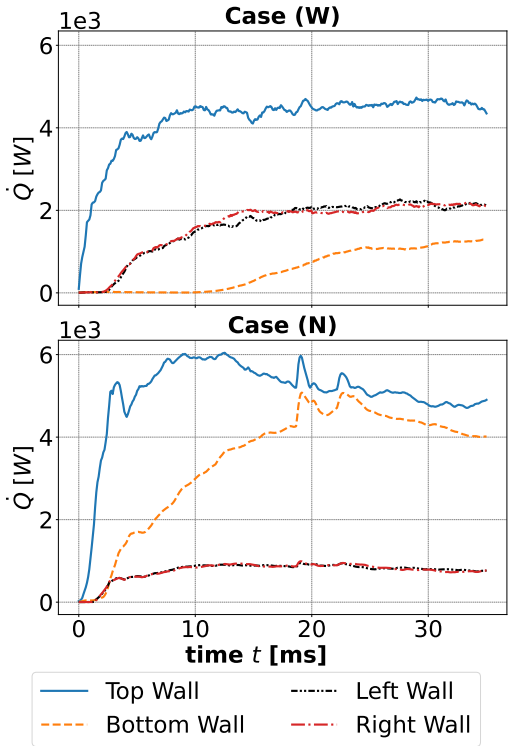

Fig. 6: Total heat ($\dot{Q}$ $[W]$) transferred to the four tunnel walls over time for cases W and N.

Figure 6 displays the total heat flux $\dot{Q}$ transferred to the four tunnel walls versus time. The heat flux $\dot{Q}$ is calculated by integrating the local heat flux provided by the wall law model over the surface A of each cell of the respective tunnel wall.

At steady state, the sum of all heat fluxes to the duct is 10.5 kW for Case N and 9.85 kW for Case W. When compared to the flame power given in Table 1, which is 65.3 kW for both Cases, it means that 16 percent of the flame power is transferred to the duct walls for Case N and 15 percent for Case W. As expected, this number is higher for the most confined case. Furthermore, while the bottom wall receives the smallest heat flux of all walls for Case W, it receives a flux comparable to the top wall for Case N, confirming that combustion is occupying the whole channel for Case N. The maximum flux for the top wall of Case N moreover indicates values 20 percent higher than for Case W.

The spatial distribution of heat flux to the tunnel walls at $t = 40$ ms, when the heat flux is fully established, is shown in Figure 7. For Case W, the heat flux to the top wall is maximum where the flame impinges the top wall, near the jet's central axis. These values decrease radially toward the tunnel sidewalls, where the flame bends downward (Fig. 4). On the sidewalls, heat transfer is concentrated near the edge of the top wall along the jet's central axis. The bottom wall, in contrast, shows a region of reduced heat transfer along the duct's central axis, flanked by areas of higher heat flux.

Case N reveals substantial differences: a central cold zone is present on the top wall, caused by the impingement of the cold, quenched jet fluid onto the ceiling so that local fluxes are smaller than for Case W. In contrast, heat transfer to the bottom wall is significantly enhanced, with high heat fluxes on the sidewalls merging near the duct floor along the jet axis. On the sidewalls, the heat flux is more evenly distributed. Finally, small-scale structures propagating along the walls are observed in Case W, though these structures are more pronounced in Case N. A video highlighting these structures is accessible via the supplementary materials.

5. Conclusion

The effects of confinement on a 1.5 mm hydrogen underexpanded jet flame (total pressure: 5 bar) into a rectangular duct with an air crossflow were simulated for two extreme confinement cases characterized by the nozzle-to-wall distance L_z: $L_z = 90$ mm (Case W: limited confinement) and $L_z = 20$ mm - (Case N: strong confinement). For Case W, L_z was larger than the expected lift-off height (L=48 mm) while it was smaller for Case N.

For Case W ($L_z = 90$ mm), LES revealed a typical underexpanded jet flame stabilization followed by wall impingement with a limited interaction: the shock structure and the flame stabilization around the hydrogen jet were almost unaffected by the following interaction of the burnt gases with the top wall. A rich premixed flame was observed in the jet core,

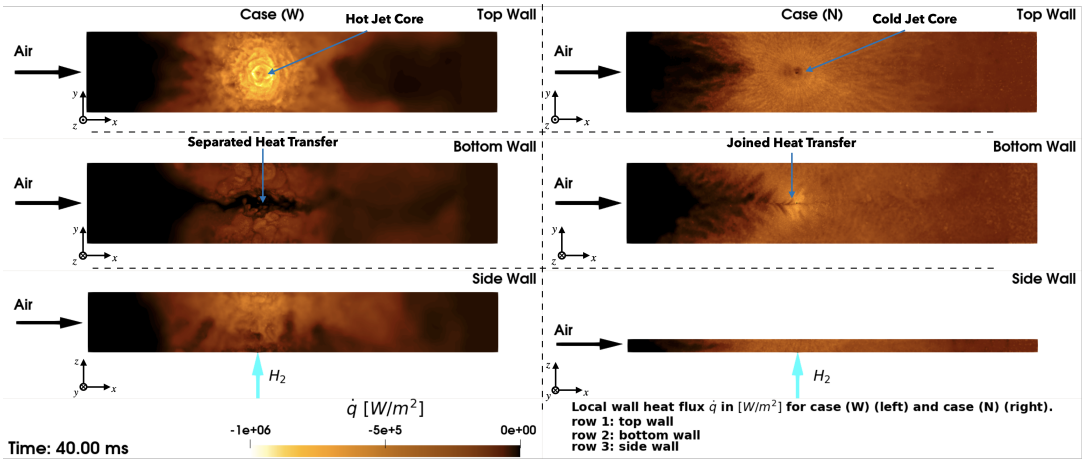

Fig. 7: Instantaneous wall heat transfer in quasi-steady state on top, bottom and side walls of the duct. Left: case W. Right: case N. A video is available in the supplementary materials.

with a trailing diffusion flame along the stoichiometric surface. The main flame remained stabilized at its lift-off height L in the absence of confinement.

For Case N ($L_z = 20$ mm), the strong confinement led to a completely different flame shape: no flame could ignite and stabilize before the jet reached the top wall. The flame is quenched on the hydrogen jet but is stabilized in a different mode. Hydrogen hit the top wall and was pushed across the tunnel walls, invading almost the whole duct and creating a large zone of rich gases surrounded by a diffusion flame. For Case W, almost all the hydrogen was burned in the duct while roughly 30 percent of unburnt hydrogen was ejected for Case N leading to another safety hazard.

In terms of safety, cases W and N led to different wall heat loads. Case W displayed typical jet flame impingement characteristics, where the highest heat transfer was found at the tunnel ceiling along the jet's central axis. This was due to the premixed flame branch producing hot gases that directly impinged the top wall. On the sidewalls, heat transfer was highest near the top wall and decreased radially downwards while on the bottom wall heat transfer remained small and did not take place in the central axis of the duct floor.

For Case N, a central cold region was observed on the top wall, resulting from unburnt, cold gases being pushed against the ceiling, where no flame could stabilize prior to reaching the duct's top wall. The sidewalls exhibited a more evenly distributed heat transfer, extending far downstream toward the outlet. On the bottom wall, hot regions converged along the central axis, producing heat levels comparable to those at the top wall. Additionally, geometrical patterns of wall heat flux were significantly finer for Case N compared to Case W, indicating a more intricate heat transfer structure. Overall, more heat flux was imposed on the duct walls for Case N than for Case W.

To validate the numerical findings presented in this study, a future comparison with experimental data is planned. Such a comparison will help assess the accuracy of the simulation results and provide deeper insights into the underlying heat transfer mechanisms observed in confined jet flame configurations.

Declaration of competing interest

The authors declare that they have no known competing financial interests or personal relationships that could have appeared to influence the work reported in this paper.

Acknowledgments

Funding from Airbus France, DGAC, France and the European Union within the project NextGenerationEU is gratefully acknowledged. No content in the paper is subject to any Export Control regulation neither of the United States of America nor the European Union. In addition, this paper does not contain any U.S. origin ITAR or EAR content. This work was performed using HPC resources from GENCI-TGCC (Grant 2023 - A0132B10157). The authors also thank Ms. F. Garnier, Dr. Q. Douasbin and Dr. T. Jaravel (CERFACS) for fruitful discussions and Dr. T. Schuller and Mr. M. Hamdaoui (IMF Toulouse) for interesting interactions on future experimental validations.

Supplementary material

Supplementary material related to this article can be found online at .

Annex 1: Grid Independence

The present flames combine shocks, choked nozzles, turbulence and chemistry so that the question of mesh independence naturally comes up. It was

tackled here for Case N by changing the resolution from 15M to 110 Mcells as follows: an initial unstructured grid displayed in Figure 8 of 15M tetrahedra is used for the simulations until a steady state is reached (based on the heat flux to the tunnel walls). The resolution of the wind tunnel is set to at least 20 points per tunnel height ($\Delta x = 1.0$ mm) and is refined around the central axis of the jet hydrogen nozzle exit where a resolution $\Delta x = 75$ μm provides 20 points per diameter. The resolution is axially and radially decreased from the nozzle exit in a linear manner to $\Delta x = 0.5$ mm at the tunnels ceiling and up to a radius of $r = 30$ mm. The refined region is coarsened linearly towards the overall tunnel resolution where $r = 30 - 60$ mm. This is the mesh used for the production runs in the paper.

A grid independence study is performed using refined grids, where the maximum edge size of the tunnel Δx_{max}^{tunnel} is decreased iteratively by a factor of two. The maximum edge size of the jet refinement is stepwise reduced to $\Delta x_{max}^{jet} = 0.25$ mm. The resolution in the nozzle is unchanged to keep the CFL-limitation constant. Results are averaged over 10 ms of physical time. The grid parameters as well as global quantities for comparison are summarized in Table 2.

Table 2: Grid Parameters and Global Variables

Description (units)	Grid 1	Grid 2	Grid 3
Number of cells	15 M	35 M	110 M
Δx_{max}^{tunnel} $[mm]$	1.0	0.5	0.25
Δx_{max}^{jet} $[mm]$	0.5	0.375	0.25
$RCT[\frac{CPUs}{node \cdot it}] \cdot 10^{-6}$	2.0	2.3	3.3
$\overline{\dot{Q}}$ $[kW/m^2]$	144	165	191
$\overline{y}^+$ $[-]$	30	27	18
y_{min}^+ $[-]$	3	2	1

Grid independence was first evaluated using global variables, such as wall heat transfer and y^+ values at the tunnel ceiling. An increase in grid resolution led to higher mean wall heat fluxes ($\overline{\dot{Q}}$), wich increases of 14% and 15% observed when moving from Grid 1 to Grid 2 and Grid 3, respectively. This behaviour is linked to changes in wall resolution, reflected in the y^+ values. Grids 1 and 2 exhibit similar mean y^+ values ($\overline{y}^+ \approx 30$), while Grid 3 achieves a finer resolution with $\overline{y}^+ \approx 18$. The lower y^+ values in Grid 3 result in a more accurate representation of near-wall gradients, explaining the higher heat flux values.

Local quantities on the central axis of the jet are relevant to verify mesh effects because they are controlled by the shock system of the underexpanded jet: axial velocity and pressure profiles are displayed in Figure 9. The position of peaks of average axial velocity as well as the peaks of pressure is the same on all three grids, confirming that the simulations are well resolved.

References

[1] R. Viskanta, Heat transfer to impinging isothermal gas and flame jets, Exp. Therm. Fluid Sci. 6 (1993).

[2] D. Bradley, J. Casal, A. Palacios, Prediction of lift-off distance in choked and subsonic hydrogen jet fires, Catal. Today 329 (2019).

[3] F. Yang, T. Wang, X. Deng, J. Dang, Z. Huang, S. Hu, Y. Li, M. Ouyang, Review on hydrogen safety issues: Incident statistics, hydrogen diffusion, and detonation process, Int. J. Hydrogen Energy. 46 (2021).

[4] L. R. Boeck, J. Hasslberger, T. Sattelmayer, Flame Acceleration in Hydrogen/Air Mixtures with Concentration Gradients, Combust. Sci. Technol. 186 (2014).

[5] L. D. Nardi, F. A. Meziat Ramirez, Y. Djebien, Q. Douasbin, O. Dounia, O. Vermorel, T. Poinsot, Detailed validation of LES for H 2 /CH 4 /Air deflagrations in an obstructed tube using PIV measurements, Combust. Flame 272 (2025).

[6] L. De Nardi, H. J. Vargas Ruiz, Q. Douasbin, O. Dounia, T. Poinsot, LES Modeling of High-Pressure Nitrogen Cross-Flow Jet Impact on Hydrogen-Air Deflagration, Proc. Combust. Inst 40 (2024).

[7] F. A. Meziat Ramirez, B. Vanbersel, O. Dounia, T. Jaravel, Q. Douasbin, O. Vermorel, Numerical study of the flame acceleration mechanisms of a lean hydrogen/air deflagration in an obstructed channel, Int. J. Hydrogen Energy. 89 (2024).

[8] R. Schefer, G. Evans, J. Zhang, A. Ruggles, R. Greif, Ignitability limits for combustion of unintended hydrogen releases: Experimental and theoretical results, Int. J. Hydrogen Energy. 36 (2011).

[9] X. Li, E. S. Hecht, D. M. Christopher, Validation of a reduced-order jet model for subsonic and underexpanded hydrogen jets, Int. J. Hydrogen Energy. 41 (2016).

[10] A. Hourri, F. Gomez, B. Angers, P. Bénard, Computational study of horizontal subsonic free jets of hydrogen: Validation and classical similarity analysis, Int. J. Hydrogen Energy. 36 (2011).

[11] C. E. Tinney, M. N. Glauser, L. S. Ukeiley, Low-dimensional characteristics of a transonic jet. Part 1. Proper orthogonal decomposition, J. Fluid Mech. 612 (2008).

[12] C. E. Tinney, L. S. Ukeiley, M. N. Glauser, Low-dimensional characteristics of a transonic jet. Part 2. Estimate and far-field prediction, J. Fluid Mech. 615 (2008).

[13] Y. Moule, V. Sabelnikov, A. Mura, Highly resolved numerical simulation of combustion in supersonic hydrogen–air coflowing jets, Combust. Flame 161 (2014).

[14] A. Edalatpour, A. Hassanvand, M. B. Gerdroodbary, R. Moradi, Y. Amini, Injection of multi hydrogen jets within cavity flameholder at supersonic flow, Int. J. Hydrogen Energy. 44 (2019).

[15] L. Prandtl, Über Die Stationären Wellen in Einem Gasstrahl, Hirzel, 1904.

[16] G. N. Abramovich, TA. Girshovich, S. I. Krasheninnikov, AN. Sekundov, IP. Smirnova, The theory of turbulent jets, Moscow Izdatel Nauka (1984).

[17] H. Martin, Heat and Mass Transfer between Impinging Gas Jets and Solid Surfaces, in: Advances in Heat Transfer, Vol. 13, Elsevier, 1977.

[18] BL. Button, D. Wilcock, Impingement heat transfer—a bibliography 1890–1975, Previews Heat Mass Transfer 4 (1978).

[19] S. J. Downs, E. H. James, Jet impingement heat transfer: A literature study (1987).

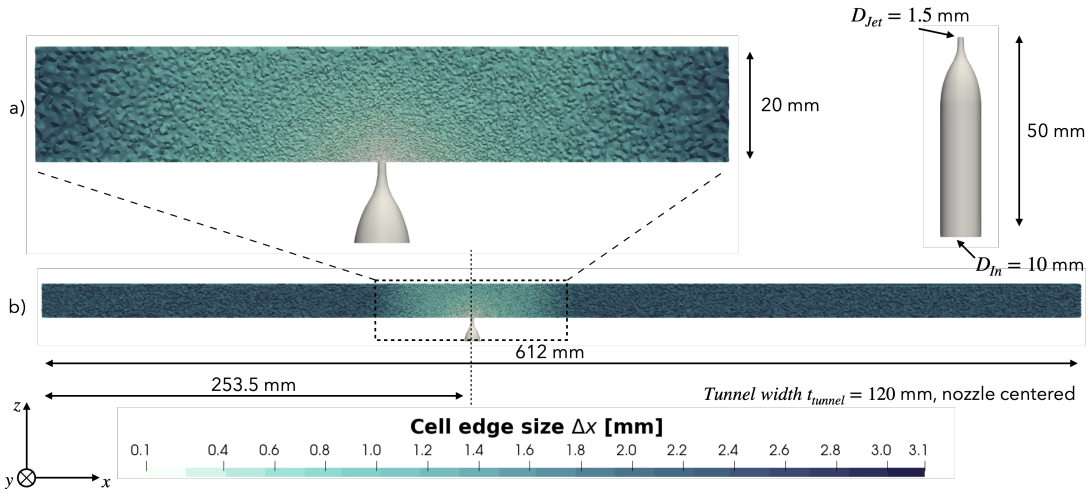

Fig. 8: Mid-plane cut (x-z plane) of the computational domain for Grid 1: a) close-up of the refined nozzle region (190 mm $< x <$ 310 mm, b) full domain, showing the transition towards larger cell sizes ($0 < x > 612$).

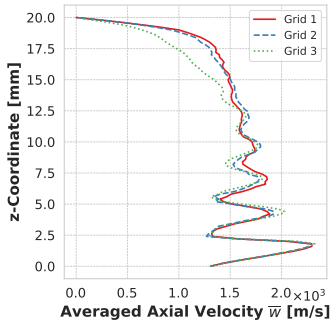

(a) Averaged z-velocity.

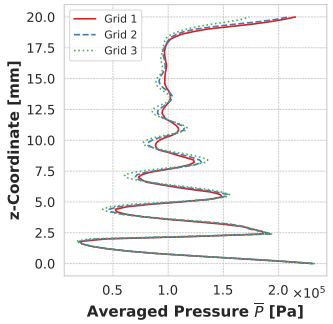

(b) Averaged pressure.

Fig. 9: Profiles of time-averaged axial velocity (top image) and pressure (bottom image) on the jet centerline for Grids 1, 2 and 3.

[20] J. Masters, CJ. Towler, PFY. Wong, The development and exploitation of rapid heating techniques, IGE J 11 (1971).

[21] V. C. Raj, P. Kuntikana, S. Sreedhara, S. Prabhu, Separation of heat transfer components from impinging methane diffusion flames, Int. J. Heat Mass Transf. 126 (2018).

[22] R. Conolly, R. Davies, A study of convective heat transfer from flames, Int. J. Heat Mass Transf. 15 (1972).

[23] A. Milson, N. Chigier, Studies of methane and methane-air flames impinging on a cold plate, Combust. Flame 21 (1973).

[24] J. K. Kilham, M. R. I. Purvis, Heat Transfer From Normally Impinging Flames, Combust. Sci. Technol. 18 (1978).

[25] M. Fairweather, J. Kilham, S. Nawaz, Stagnation point heat transfer from laminar, high temperature methane flames, Int. J. Heat Fluid Flow 5 (1984).

[26] J. N. Livingood, P. Hrycak, Impingement heat transfer from turbulent air jets to flat plates: A literature survey (1973).

[27] D. Lytle, Secondary heat transfer maxima for air jet impingement at low nozzle-to-plate spacing, Exp. Heat Transf. (1991).

[28] G. Hargrave, M. Fairweather, J. Kilham, Forced convective heat transfer from premixed flames, Int. J. Heat Fluid Flow 8 (1987).

[29] J. Bee´r, N. Chigier, Impinging jet flames, Combust. Flame 12 (1968).

[30] R. Germerdonk, Über die Größe des konvektiven Wärmeübergangs von der Flamme auf das Glas in Glasschmelzwannenöfen, Teil I u. II, Glastech. Ber 36 (1963).

[31] J. X. Wen, E. S. Hecht, R. Mevel, Recent advances in combustion science related to hydrogen safety, Progress in Energy and Combustion Science 107 (2025).

[32] D. Bradley, P. H. Gaskell, X. Gu, A. Palacios, Jet flame heights, lift-off distances, and mean flame surface density for extensive ranges of fuels and flow rates, Combust. Flame 164 (2016).

[33] K. A. Phalnikar, R. Kumar, F. S. Alvi, Experiments on free and impinging supersonic microjets, Exp. Fluids 44 (2008).

[34] T. Schonfeld, M. Rudgyard, Steady and Unsteady Flow Simulations Using the Hybrid Flow Solver AVBP, AIAA J. 37 (1999).

[35] O. Colin, M. Rudgyard, Development of High-Order Taylor–Galerkin Schemes for LES, J. Comput. Phys. 162 (2000).
[36] F. Nicoud, F. Ducros, Subgrid-Scale Stress Modelling Based on the Square of the Velocity Gradient Tensor, Flow Turbul. Combust. 62 (1999).
[37] O. Colin, Simulations Aux Grandes Echelles de la Combustion Turbulente Premelangee das les Statoreacteurs, Ph.D. thesis, Institut Polytechnique de Toulouse, Toulouse (2000).
[38] T. Schmitt, Large-Eddy Simulations of the Mascotte Test Cases Operating at Supercritical Pressure, Flow Turbul. Combust. 105 (2020).
[39] P. Saxena, F. A. Williams, Testing a small detailed chemical-kinetic mechanism for the combustion of hydrogen and carbon monoxide, Combust. Flame 145 (2006).
[40] T. Jaravel, Prediction of pollutants in gas turbines using large eddy simulation, Ph.D. thesis, Institut Polytechnique de Toulouse, Toulouse (2016).
[41] F. Charlette, C. Meneveau, D. Veynante, A power-law flame wrinkling model for LES of premixed turbulent combustion Part I: Non-dynamic formulation and initial tests, Combust. Flame 131 (2002).
[42] A. Aniello, D. Laera, L. Berger, A. Attili, T. Poinsot, Introducing thermodiffusive effects in large-eddy simulation of turbulent combustion for lean hydrogen-air flames, Center for Turbulence Research, Proceedings of the Summer Program (2022).
[43] H. Vargas Ruiz, D. Laera, G. Lartigue, S. Mashruk, A. Valera-Medina, L. Gicquel, Extension of the dynamic Thickened Flame model for partially-premixed multi-fuel multi-injection combustion and application to an ammonia–hydrogen swirled flame, Combust. Flame 274 (2025).
[44] E. Lo Schiavo, D. Laera, E. Riber, L. Gicquel, T. Poinsot, Effects of liquid fuel/wall interaction on thermoacoustic instabilities in swirling spray flames, Combust. Flame 219 (2020).
[45] D. Laera, P. Agostinelli, L. Selle, Q. Cazères, G. Oztarlik, T. Schuller, L. Gicquel, T. Poinsot, Stabilization mechanisms of CH4 premixed swirled flame enriched with a non-premixed hydrogen injection, Proc. Combust. Inst 38 (2021).
[46] A. Aniello, D. Laera, S. Marragou, H. Magnes, L. Selle, T. Schuller, T. Poinsot, Experimental and numerical investigation of two flame stabilization regimes observed in a dual swirl H 2 -air coaxial injector, Combust. Flame 249 (2023).
[47] L. Gaipl, T. Jaravel, Q. Douasbin, T. Poinsot, LES of the combustion efficiency of wake stabilized methane jet flames in crossflow, Combust. Flame 273 (2025).
[48] H. Yamashita, M. Shimada, T. Takeno, A numerical study on flame stability at the transition point of jet diffusion flames, Symp. (Int.) Combust. 26 (1996).
[49] T. J. Poinsot, S. K. Lele, Boundary Conditions for Direct Simulations of Compressible Viscous Flows, J. Comput. Phys. 101 (1992).
[50] E. R. Van Driest, Turbulent Boundary Layer in Compressible Fluids, Journal of the Aeronautical Sciences 18 (1951).
[51] B. Kader, Temperature and concentration profiles in fully turbulent boundary layers, Int. J. Heat Mass Transf. 24 (1981).
[52] T. Poinsot, D. Veynante, Theoretical and Numerical Combustion, 3rd Edition, CNRS, Toulouse, 2011.
[53] S. R. Gollahalli, B. Nanjundappa, Burner Wake Stabilized Gas Jet Flames in Cross-Flow, Combust. Sci. Technol. 109 (1995).